

High strength and ductility of an additively manufactured CrCoNi medium-entropy alloy achieved by minor Mo doping

Jiaying Wang¹, Jianpeng Zou¹, Hailin Yang^{1,*}, Zhilin Liu², Shouxun Ji³

1. State Key Laboratory of Powder Metallurgy, Central South University, Changsha 410083, China

2. Light Alloy Research Institute, College of Mechanical and Electrical Engineering, Central South University, Changsha, 410083, P.R. China

3. Brunel Centre for Advanced Solidification Technology (BCAST), Brunel University London, Uxbridge, Middlesex, UB8 3PH, United Kingdom

** Corresponding author: y-hailin@csu.edu.cn*

Abstract: Selective laser melting (SLM) of a (CoCrNi)₉₅Mo₅ medium-entropy alloy (MEA) is explored to architect the dislocation-formed sub-grains and ultrafine μ precipitates. The high strength and ductility were achieved in the as-SLMed (CoCrNi)₉₅Mo₅ alloy, where the yield strength, ultimate tensile strength (UTS) and fracture strain were \sim 0.79 GPa, \sim 0.97 GPa and 35.9%, respectively. These excellent mechanical properties mainly originated from the hierarchical microstructures being composed of high-density dislocations-formed equiaxed cellular structures, low-angle grain boundaries (LAGBs) within the columnar cellular structures, fine (Mo, Cr)-enriched μ precipitates, and the lattice defects (i.e. dislocations, stacking faults and Lomer-Cottrell locks). In addition, the formation of low-density semi-coherent μ nanoprecipitates also enhanced the strengthening and minimized the loss of ductility in the (CoCrNi)₉₅Mo₅ MEA.

Keywords: CoCrNi medium-entropy alloy; Selective laser melting; Hierarchical microstructure; Mechanical properties; Precipitate strengthening

1. Introduction

CoCrNi medium-entropy alloy (MEA) delivers excellent ductility and fracture toughness at room and/or cryogenic scenario [1–3]. Unfortunately, the pure as-cast/as-sintering CoCrNi MEA with low strength (yield strength normally lower than 400 MPa) becomes insufficient for many engineering applications. Several essential technical developments have been carried out to improve the mechanical properties for specified requirements [2, 4–7].

Taking the nature of simple solid solution of MEAs in consideration, the significant enhancement in strength of MEAs through solid solution strengthening/precipitation strengthening is attractive and the progresses have been successfully made for a number of systems. For instance, the crystal structures of CoCrNi alloy can be tuned by adding Mo atoms, which can form the high degree of lattice distortion and precipitates (σ and μ), leading to the impediment to dislocation movement [8, 9]. Unfortunately, the semi-coherent interface between face-center cubic (fcc) matrix and high-density σ/μ precipitates tends to weaken ductility significantly [8, 9]. Moreover, the size of σ/μ precipitates introduced by single conventional casting and/or spark plasma sintering (SPS) method is relatively coarsening (i.e. 1~2 μm for casting [10], and ~500 nm for SPS [8]), which need to be refined by subsequent plastic deformation.

Recently, selective laser melting (SLM) is used to develop high-performance and complex structural materials at a high cooling rate up to 10^5 – 10^6 °C/s [11–13]. The SLM process is an innovative method suitable for fabricating metallic materials such as Al-based alloys [12,13], Ti-based alloys [14], Fe-based alloys (steels) [15], Ni-based alloys [16], and HEAs/MEAs [17–19]. Particularly, for the precipitation-strengthening alloys fabricated by SLM, such as Al alloys reinforced by Mg_2Si precipitates [13] and Ni superalloys reinforced by γ' precipitates [16], the ultrafine sizes induced by high cooling rate deliver excellent precipitation strengthening and mechanical properties. Additionally, rapid cooling during solidification also increases the solute solubility in matrix, which can lead to an obvious increase in solid solution strengthening. However, the microstructures and mechanical properties of precipitation-strengthening CoCrNi-Mo alloy still remains unclear regarding SLM process.

In this work, it is aimed to explore the microstructural evolution and mechanical response of the SLMed CoCrNi MEA doped by 5 at% Mo. The manufacturing process was optimized to generate the special microstructures required for excellent mechanical properties in the $(\text{CoCrNi})_{95}\text{Mo}_5$ alloy. The discussion focuses on the relationship between the microstructures and mechanical properties in association with the corresponding strengthening mechanisms.

2. Materials and methods

2.1 Powder and materials fabrication

Pre-alloyed (CrCoNi)₉₅Mo₅ powders with a particle size distribution of 15~53 μm were made in house and used for additive manufacturing of SLM in this work. Inductively coupled plasma atomic emission spectrometry (ICAP 7000 Series) was used to analyse the chemical composition of powders in Table 1. No composition segregation was detected within pre-alloyed powder with a spherical morphology, as showing in in Fig. 1. The SLM process was conducted using a FS271M (Farsoon, Inc, China) machine. The parameters were adopted with a laser powder (P) of 400 W, scan speed (v) of 600 to 1200 mm/s, hatch spacing (h) of 0.12 mm, and layer thickness (t) of 0.04 mm. Particularly, the volume energy density (VED) of SLM mode is calculated based on Eq. (1):

$$VED = P / (vht) \quad (1)$$

Correspondingly, The $VEDs$ adopted in this study are 69.4 J/mm³, 83.3 J/mm³, 104.2 J/mm³ and 138.8 J/mm³, respectively. Additionally, the laser scanning strategy was used 67° rotating scanning layer-by-layer. The detailed scanning strategy diagram and optical micrograph of the SLM samples are shown in Fig. 2a and 2b, respectively.

Table 1. Chemical Compositions of the (CoCrNi)₉₅Mo₅ pre-alloyed powder (wt.%).

| Element | Co | Cr | Ni | Mo | Fe | C | O | N | S |
|---------|------|------|------|-----|-------|--------|--------|--------|--------|
| wt.% | 33.1 | 28.1 | 33.4 | 5.3 | 0.069 | 0.0068 | 0.0164 | 0.0041 | 0.0036 |

2.2 Microstructure characterization

The crystal structure of alloys under different conditions was examined by X-ray diffraction technique with Cu $K\alpha$ radiation (XRD, Rigaku). Microstructure evolution of the alloy was examined by scanning electron microscope (SEM), an electron backscattered diffraction (EBSD, FIB Helios NanoLab G3 UC) equipped with the TSL OIM data analysis software, and a transmission electron microscope (TEM; Titan G2 60-300). Before EBSD and XRD characterization, the samples were firstly ground with SiC papers diamond suspensions and then polished using 40 nm colloidal silica suspension. TEM samples were prepared using the precision ion polishing system (PIPS) at a voltage of 5 kV/2 kV and an incident angle of 3° ~ 7°.

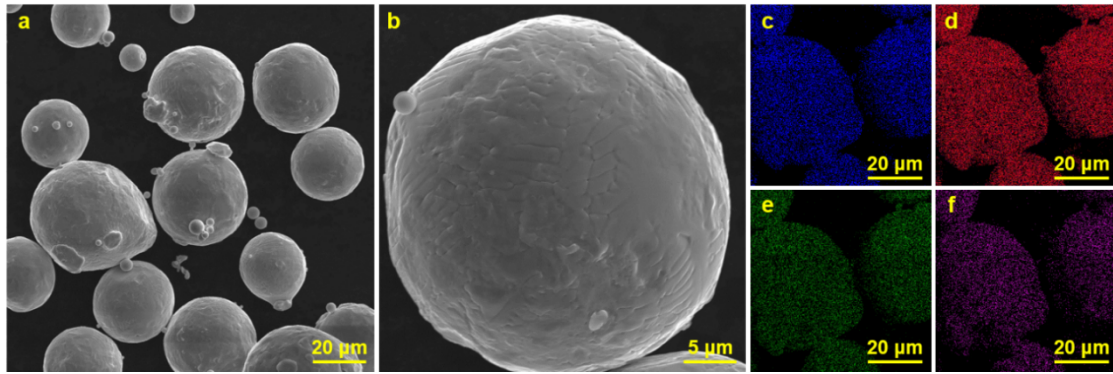


Fig. 1. Characterization of pre-alloyed $(\text{CoCrNi})_{95}\text{Mo}_5$ MEA powder: (a)-(b) Powder particle morphology, and (c)-(f) Energy-dispersive spectrometer (EDS) mapping for different major elements.

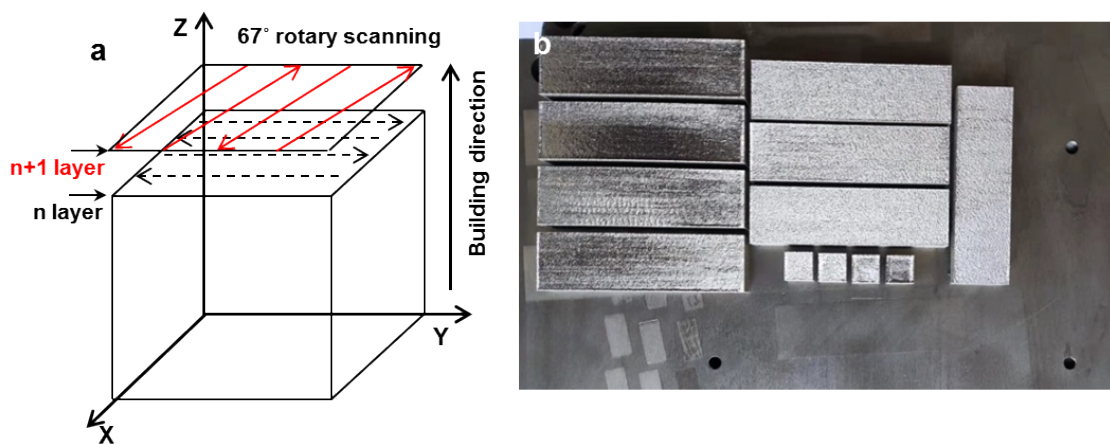


Fig. 2. (a) Schematic diagram of laser beam scanning procedure during SLM fabricating process; (b) optical micrographs, showing the sample obtained from SLM for parameter optimization.

2.3 Mechanical testing

Dog-bone-shaped with a gauge length of 30 mm and square shaped samples ($10\text{ mm} \times 10\text{ mm} \times 2\text{ mm}$) were used for tensile testing and micro-hardness testing, respectively. The uniaxial tensile deformation was performed at room temperature using a MTS Alliance RT30 system. Hardness test was evaluated by Vickers hardness (ASTM E384-08) under a load of 300 g for 10 s. All the reported data are the average value of at least 5 measurements.

3. Results

3.1 Microstructural feature

Tensile curves of the as-SLMed $(\text{CoCrNi})_{95}\text{Mo}_5$ alloys are shown in Fig. 3a, and the corresponding data for tensile and hardness are shown in Table 2. It can be seen that the yield strength and UTS under different VEDs were nearly the same, at a relatively high value of 0.79~0.80 GPa and 0.96~0.99 GPa, respectively. Meanwhile, the fracture strain gradually

increased with increasing the VED, peaking at 35.9% under the condition of 138.8 J/mm³. Also, Fig. 1(b) shows a comparison of tensile data of CoCrNi-Mo alloys fabricated between in this study and other methods (including SPS, casting and CoCrNi alloys fabricated by casting, SPS and SLM) [1,2,4,6,8,18–20]. Obviously, the alloys fabricated in the present work exhibited in a strong manner than the CoCrNi alloys and the CoCrNi-Mo alloys fabricated by other methods.

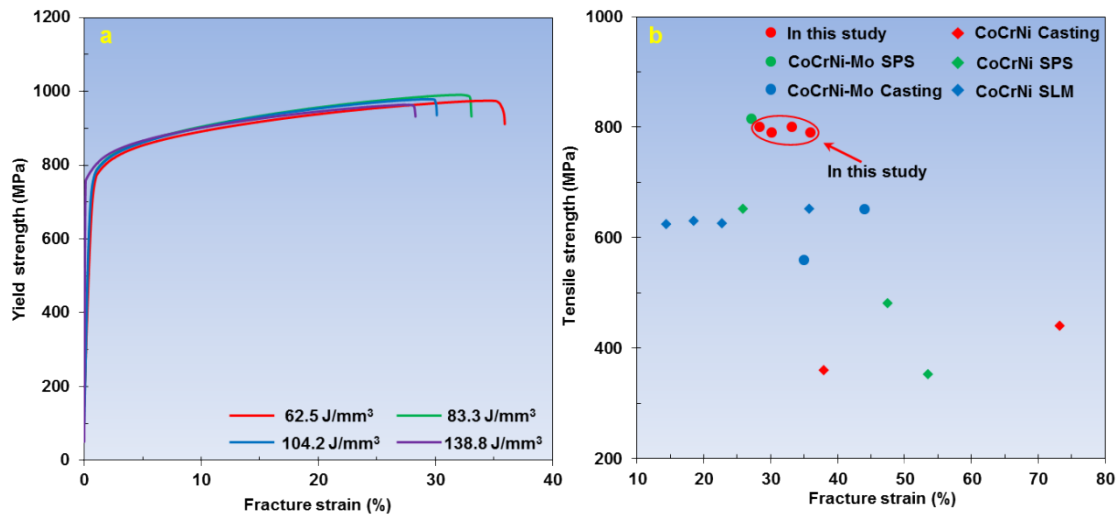


Fig. 3. (a) Tensile stress–strain curves of the as-SLMed (CoCrNi)₉₅Mo₅ alloys with different VEDs, including 69.4 J/mm³, 83.3 J/mm³, 104.2 J/mm³ and 138.8 J/mm³; (b) Comparison of tensile properties between the as-SLMed CoCrNi-Mo alloys fabricated in this study and CoCrNi and CoCrNi-Mo alloys fabricated by other methods [1,2,4,6,8,18–20].

Table 2 The yield strength (YS), ultimate tensile strength (UTS), fracture strain (FS), and Vickers hardness determined for SLM (CoCrNi)₉₅Mo₅ alloys with different VEDs.

| VED (J/mm ³) | YS (GPa) | UTS (GPa) | FS (%) | Hardness (Hv) |
|--------------------------|----------|-----------|--------|---------------|
| 69.4 | 0.79 | 0.96 | 28.3 | 281.6 |
| 83.3 | 0.80 | 0.98 | 30.1 | 275.6 |
| 104.2 | 0.80 | 0.99 | 33.1 | 282.3 |
| 138.8 | 0.79 | 0.97 | 35.9 | 277.8 |

Fig. 4 depicts the microstructure of the as-SLMed (CoCrNi)₉₅Mo₅ alloy under different VEDs in the top view (a-d) and side view (e-h). Obviously, the thickness of scanning layer in microstructure was about 120 μm (Fig. 4b), which was consistent with the value pre-set in the machine. Additionally, cracks could be detected as marked by the yellow arrows and the density of cracks decreased with increasing the VEDs (almost no cracks were observed when VED exceeded 104.2 J/mm³). Additionally, there were more cracks on the top view than that at the side view. Also, only equiaxial grains were detected in the top view and elongated columnar grains that expanded to multiple building layers in the side view due to the rapid

cooling rate and thermal cycling of the melting pool during SLM process [21].

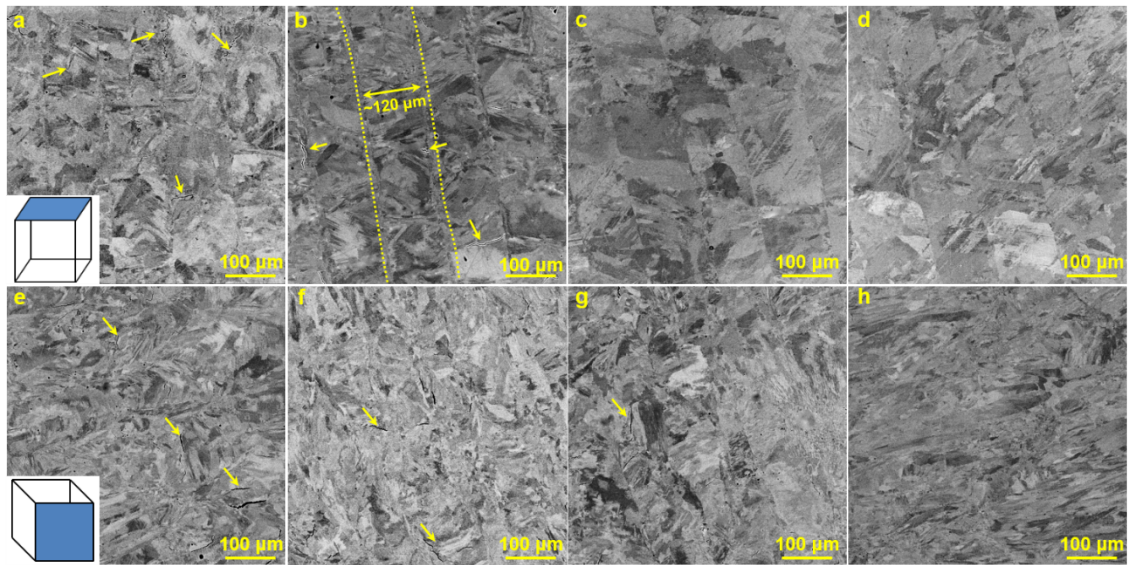


Fig. 4. SEM/BSE of SLMed (CoCrNi)₉₅Mo₅ alloys on (a)-(d) the top view and (e)-(h) the side view with the different VEDs, including (a) and (e) 69.4 J/mm³, (b) and (f) 83.3 J/mm³, (c) and (g) 104.2 J/mm³, and (d) and (h) 138.8 J/mm³. Note: the yellow arrows indicate the formation of cracks.

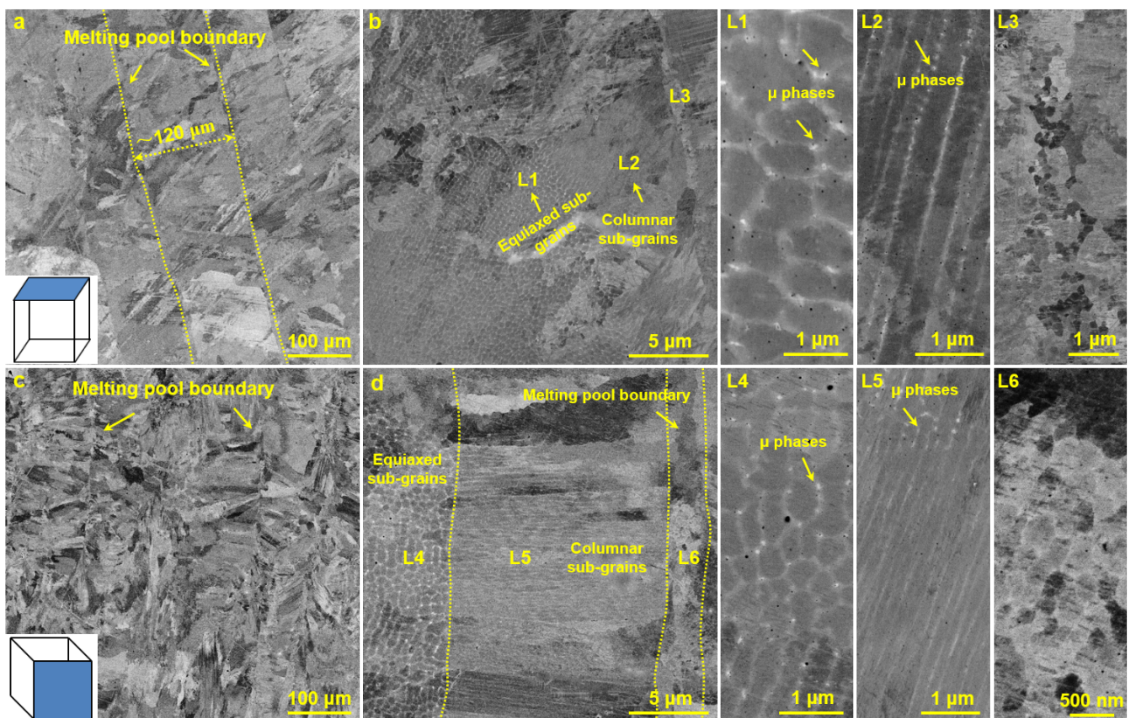


Fig. 5. SEM/BSE images showing the detailed microstructure of SLMed (CoCrNi)₉₅Mo₅ alloys under the condition of 138.8 J/mm³; (a) the overall microstructure in the top view; (b) the hierarchical microstructure consisted of columnar and equiaxed sub-grains; (L1) – (L3) the detailed microstructure of equiaxed sub-grains, columnar sub-grains and equiaxed grains distributed near scanning tracks, respectively; (c) the overall microstructure in side view; (d) the hierarchical microstructure consisted of columnar and equiaxed sub-grains; (L4) – (L6) the detailed microstructure of equiaxed sub-grains, columnar sub-grains and equiaxed

grains distributed near scanning tracks, respectively.

Furthermore, the detailed microstructures along the two directions in the alloys are shown in Fig. 5. The microstructure acquired under backscattering mode (Fig. 5a-d) identified the formation of hierarchical microstructure in both views. In the top view, relatively coarse grains showed the mixture of equiaxed and columnar sub-grains. The sizes of columnar sub-grains were from dozens to hundreds of microns in length and at a level of 0.3~0.5 μm in width, while the size of equiaxed sub-grains was measured to be 0.5~1 μm , as indicated in L1&L2 in Fig.5. In the side view, the microstructure was also consisted of fine equiaxed and columnar sub-grains with melting pool boundary (Fig. 5c&d). the majority of grains runs throughout the melting pool boundary that composed of equiaxed grains (L3 and L6) and towards the centre of the melting track in both views, suggesting the epitaxial growth of these grains. Additionally, low-density nano-scale μ precipitates were observed at the boundaries of equiaxed and columnar sub-grains, as shown in the yellow arrow in L1&L2 and L4&L5 in Fig. 5, respectively.

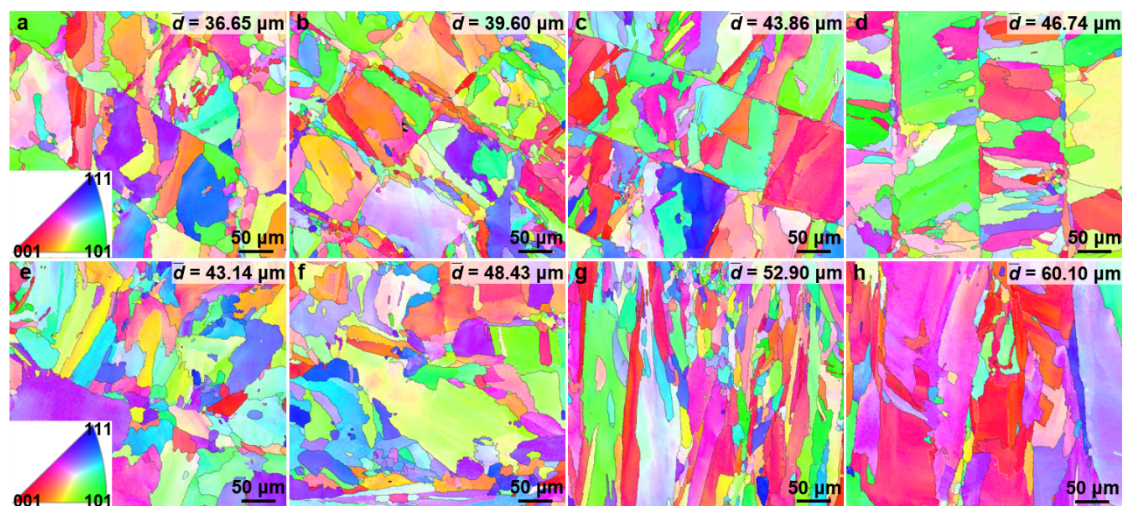


Fig. 6. Inverse pole figures (IPF) of the as-SLM $(\text{CoCrNi})_{95}\text{Mo}_5$ samples with different VEDs in the top view and side view. (a) – (d): Top view of 69.4 J/mm^3 , 83.3 J/mm^3 , 104.2 J/mm^3 and 138.8 J/mm^3 , respectively; (e) – (h): side view of 69.4 J/mm^3 , 83.3 J/mm^3 , 104.2 J/mm^3 and 138.8 J/mm^3 , respectively.

EBSD was further carried out to analyse the microstructural evolution of the as-SLM $(\text{CoCrNi})_{95}\text{Mo}_5$ alloy under different VEDs. It is obviously that the average grain size of alloy increased with increasing the VED in both views. The scanning tracks were clearly aligned with scanning direction between the two consecutive layers of 67° , as indicated in the top view (Fig. 6a-d). Similar to the results of SEM, the thickness of scanning layer in microstructure was about 120 μm , like the hatch spacing. Additionally, the centres and boundaries of scanning track were composed of columnar and equiaxed grains due to the typical Gaussian distribution of the laser energy [22, 23]. In the side view (Fig. 6e-h), the grain turned from an epitaxial to

columnar grains gradually as the VED increases. This unique microstructure was mainly affected by the thermal gradients and cooling rate, which were strongly linked to the printing parameters. Meanwhile, the shapes of melt pool were closely related to VEDs, a higher VED resulted in a wider and deeper melting pool. For the alloy fabricated by SLM, the grain grew towards the centre of melting pool in the direction perpendicular to the melting pool boundary. Thus, the preferred orientation of grains in side view should be strongly related to the VED.

Further, XRD spectra in Fig. 7 identified the existence of only single fcc phase in the alloys (side view) under different VEDs. Similarly, a strong growth texture of $\langle 100 \rangle$ was observed at the evident $\{200\}$ peak in the alloy samples with increasing the VED. To elucidate this point, the $\{200\}$ peak is equal to $\{100\}$ orientation owing to the extinction phenomenon during the XRD calibration process of disordered solid solution in fcc metals.

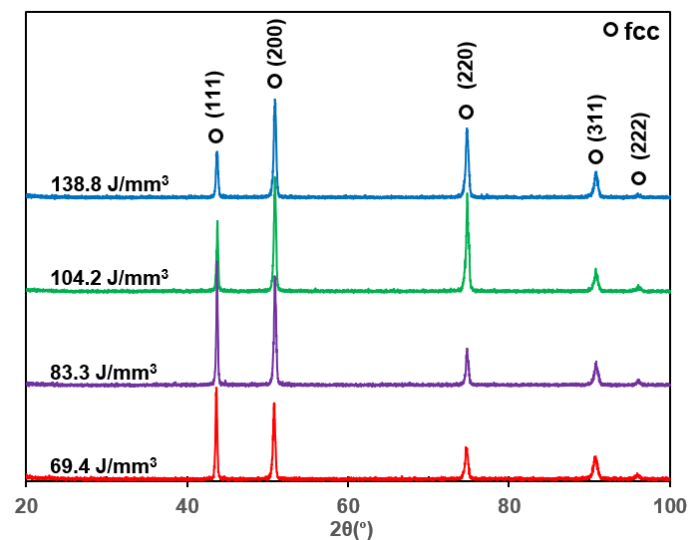


Fig. 7. XRD spectra of as-SLMed $(\text{CoCrNi})_{95}\text{Mo}_5$ alloys under different VEDs, including 69.4 J/mm^3 , 83.3 J/mm^3 , 104.2 J/mm^3 and 138.8 J/mm^3 .

4. Discussion

TEM analysis of as-SLMed $(\text{CoCrNi})_{95}\text{Mo}_5$ alloys under the condition of 138.8 J/mm^3 are shown in Fig. 8. Irregular sub-grains consisted of dislocations were shown in TEM bright-field (BF) image (Fig. 8a) and STEM image (Fig. 8b). Corresponding, the formation of unique high-density dislocation-formed sub grains in the SLMed $(\text{CoCrNi})_{95}\text{Mo}_5$ alloys possesses outstanding dislocation strengthening. Meanwhile, the columnar sub-grains were observed in the BF-TEM image (Fig. 8c) and STEM image (Fig. 8d). Particularly, the formation of nanoscale μ precipitates ($\sim 80 \text{ nm}$) were detected in the boundaries of equiaxed and columnar sub-grains. Compared with the CoCrNi-Mo alloys fabricated by casting/sintering, two

differences were found in the *in-situ* μ precipitates in the as-SLMed alloy: (i) the much lower density than that in the SPS state and cast with rolling/annealing process, (ii) the size is significantly lower than in the SPS and cast states, which is closely related with the rapid cooling rate during SLM process. Further, HR-TEM image and SAED pattern of the *in-situ* μ precipitates are shown in Fig. 8e and L1. Obviously, SAED pattern analysis of the μ precipitates that were taken along the $[\bar{1}2\bar{1}1]$ zone axes, confirmed that the phases adopt hexagonal close-packed (HCP) structure. The SEAD pattern L1 also indicated that a semi-coherent interface can be characterized between fcc matrix and μ precipitates.

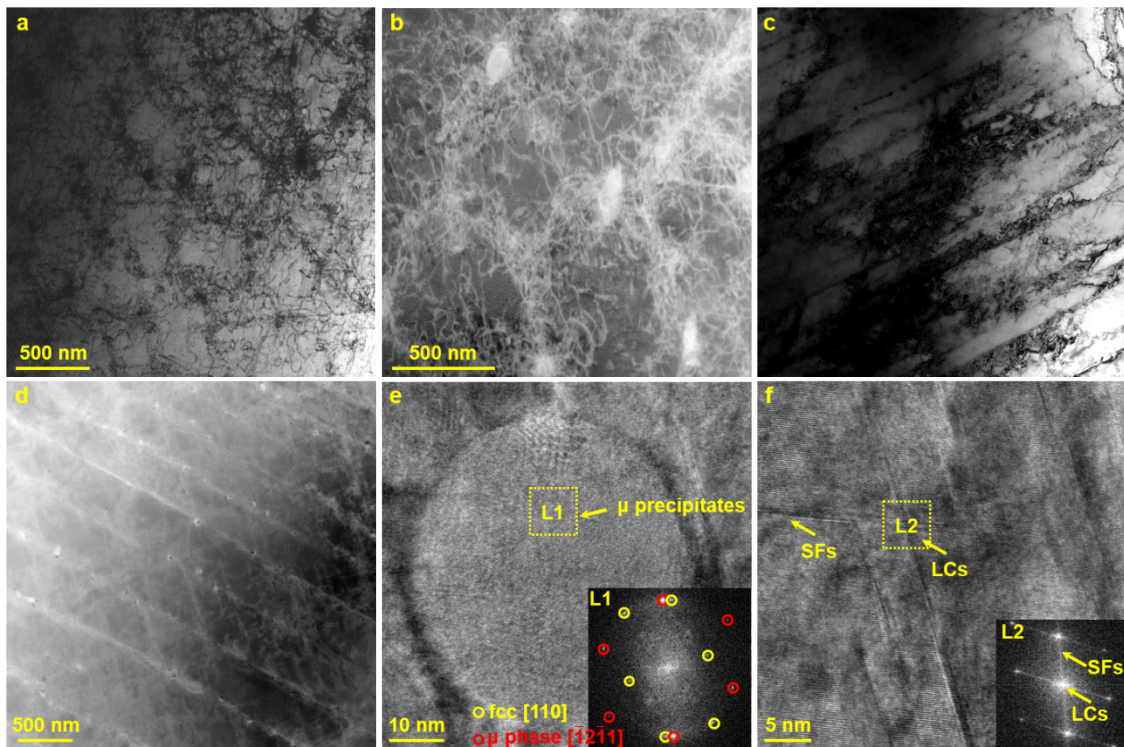


Fig. 8. TEM micrographs showing the microstructure of SLMed $(\text{CoCrNi})_{95}\text{Mo}_5$ alloys under the condition of 138.8 J/mm^3 : (a) TEM image and (b) STEM image of a high-density dislocation-formed equiaxed sub-grains; (c) TEM image and (d) STEM image of the columnar sub-grains; (e) HR-TEM image and SEAD pattern L1 showing the semi-coherent interface between fcc matrix and μ precipitate; (f) HR-TEM image showing the formation of SFs and LCs.

The chemical composition of the equiaxed and columnar sub-grains in the alloy was conducted using STEM-EDS. The compositional mapping in Fig. 9 showed that μ precipitates were enriched in Mo and Cr, but depleted in Co and Ni. Similarly, the boundaries of columnar sub-grains were enriched in Mo and Cr. Moreover, SFs were detected in the alloy, and moved and interacted while nucleating and growing from fcc matrix, leading to the formation of Lomer-Cottrell locks, as shown in the HR-TEM image of Fig. 8f. The high-density SFs formed

decrease the free pathways for dislocation movement and could enable the dynamic Hall-Petch effect, and Lomer-Cottrell locks have been considered to play a key role in the strengthening and strain hardening of MEAs/HEAs [24–27].

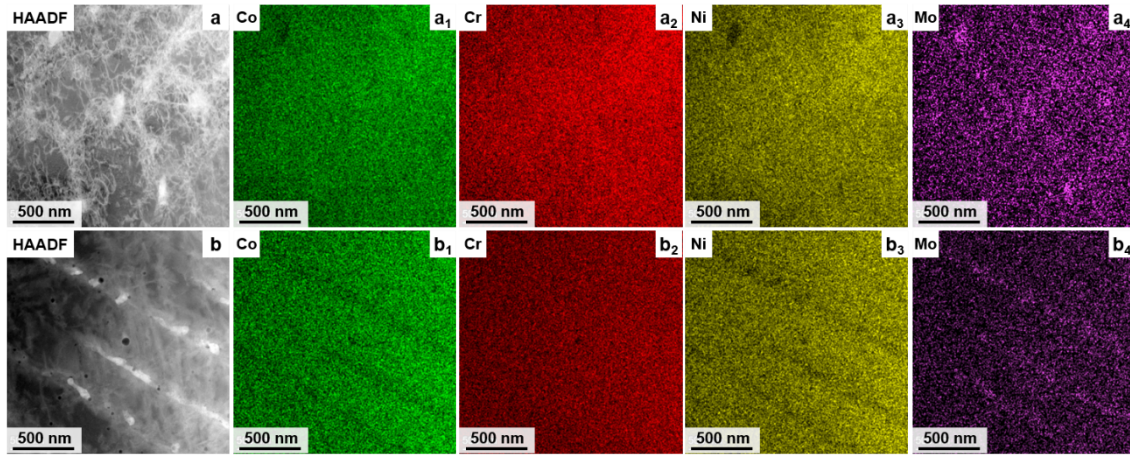


Fig. 9. (a) HAADF micrograph of equiaxed sub-grains with (a₁) – (a₄) EDS mapping of different major elements; (b) HAADF micrograph of columnar sub-grains with (b₁) – (b₄) EDS mapping of different major elements.

As mentioned above, like CoCrNi-Mo alloys fabricated by other methods, such as casting and SPS, the corresponding strengthening contributions of as-SLMed (CoCrNi)₉₅Mo₅ alloy mainly depend on solid solution strengthening (σ_s), grain boundary strengthening (σ_g), dislocation strengthening (σ_{dis}) and precipitation strengthening (σ_p). Therefore, the contribution of main mechanisms responsible for strengthening of the alloy can be expressed as:

$$\sigma_y = \sigma_0 + \sigma_s + \sigma_g + \sigma_{dis} + \sigma_p \quad (2)$$

where friction stress of σ_0 is a constant (218 MPa for CoCrNi alloy [28]). The contribution of grain refinement (σ_g) can be computed by the Hall-Petch equation [29]:

$$\sigma_g = Kd^{0.5} \quad (3)$$

where K is a constant (265 MPa· $\mu\text{m}^{1/2}$ for CoCrNi alloy [28]), As for the average grain size d of as-SLMed (CoCrNi)₉₅Mo₅ alloy, the grain boundary strengthening is referred to the dislocation motion impeded by lattice misfit and intragranular misorientation instead of the dislocation entanglement at sub-grains. Thus, the coarser grains separated by HAGBs should be taken into account while computing d . As shown in Fig. 6a, the microstructure of the as-SLMed alloy under the condition of 138.8J/mm³ mainly contains grains with an average grain size of 46.74 μm . Therefore, the yield strength contribution induced by grain refinement is estimated to be 38.8 MPa. Additionally, the contribution of dislocation strengthening can be calculated based on the Taylor's hardening law in Eq. (4) [30]:

$$\sigma_{dis} = M \cdot \alpha \cdot G \cdot b \cdot \rho^{0.5} \quad (4)$$

where M , α , G , b , and ρ are the Taylor factor, empirical constant, shear modulus, Burgers vector, and dislocation density, respectively. For the CoCrNi alloy, those parameters are $M = 3.06$ [31], $\alpha = 0.2$ [32], $G = 85$ GPa [8], $b = 0.253$ nm [33].

According to the strengthening analysis of SLM-built CrMnFeCoNi alloys carried out by Zhu et al. [17] and Kocks [30], the dislocation density is strongly correlated with the size λ of dislocation formed sub-grains (~ 450 nm, based on TEM results) in Eq. (5):

$$\sqrt{\rho} = c / \lambda \quad (5)$$

where c is a constant with $\alpha c \approx 1$ [16, 30]. Thus, the contribution of dislocation strengthening is approximately 145.3 MPa. Thus, the contribution of friction stress σ_0 , plus grain boundary strengthening (σ_g) and dislocation strengthening (σ_d) is about ~ 402 MPa.

Probably, the strength and ductility can be further enhanced via tuning volume fraction and size of the μ precipitates through optimizing the subsequent deformation and/or annealing treatments, corresponding systematically research will be presented in the future. In this study, the relatively low-density ultrafine μ precipitates induced by high cooling rate during SLM process may not deliver superior precipitation strengthening effect, while two obvious advantages were achieved in the as-SLMed alloy: (i) the low-density fine precipitates can contribute to the enhancement of solid solution strengthening due to the solution of high fraction Mo with largest metallic radius in Co-Cr-Ni-Mo alloy system. As it is hard to measure the volume fraction of μ precipitates, we cannot compute the contribution of solid solution strengthening and precipitation strengthening accurately. Considering the yield strength of ~ 0.79 GPa, the contributions of solid solution strengthening and precipitation strengthening induced by introduction of Mo is about ~ 388 MPa (for simplicity, extra contribution of lattice defects (i.e. SFs and LCs) were not considered); (ii) the formation of low-density (Mo,Cr)-enriched μ precipitates that have a semi-coherent interface with fcc matrix could minimize the loss of ductility to a large extent, which brings a relatively good fracture strain of 35.9%.

Considering the characteristics of microstructure, a representative diagram containing hierarchical microstructures in the studied (CoCrNi)₉₅Mo₅ alloy is schematically illustrated in Fig. 10. The improved strength is not only induced by the hierarchical microstructures that contain fine grain structure, dislocation-formed equiaxed sub-grains and fine columnar sub-grains segregated by LAGBs, but also by the *in-situ* μ precipitates and the boundaries formed by the SFs and LCs to inhibit the movement of high-density dislocations. Meanwhile, the formation of low-density fine (Mo, Cr)-enriched μ precipitates can minimize the loss of ductility and enhance the solution of Mo element simultaneously.

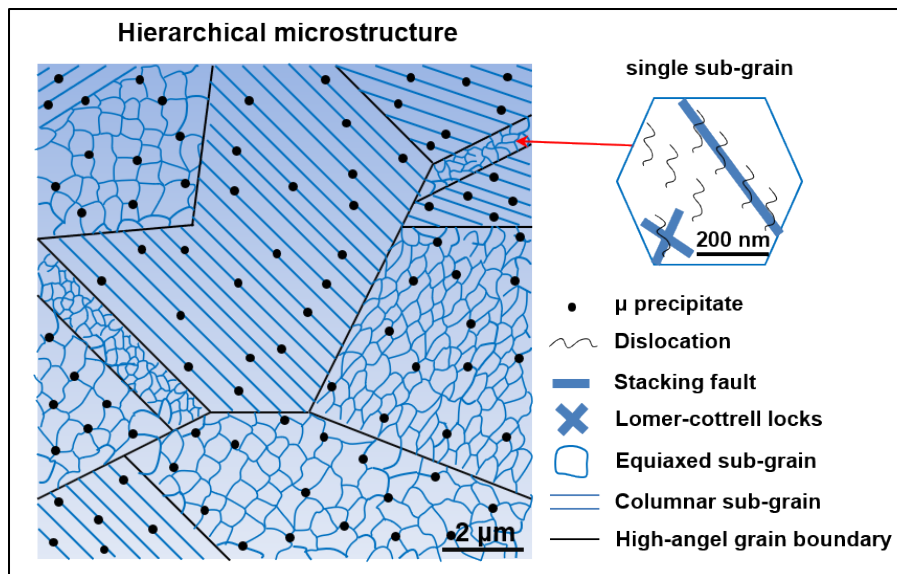


Fig. 10. Schematic diagram showing the hierarchical microstructural constituents of as-SLMed $(\text{CoCrNi})_{95}\text{Mo}_5$ alloy.

5. Conclusions

(1) The $(\text{CoCrNi})_{95}\text{Mo}_5$ medium-entropy alloy can be effectively processed by selective laser melting to produce the typical dislocation-formed sub-grains, ultra-fine μ precipitates and highly saturated solid solution of Mo in the hierarchical microstructures.

(2) The as-SLMed $(\text{CoCrNi})_{95}\text{Mo}_5$ alloy delivered the yield strength of 0.79 GPa, ultimate tensile strength of 0.97 GPa, and fracture strain of 35.9%. The evident improvement in strength mainly depends on the hierarchical microstructures composed of the high-density dislocations-formed equiaxed sub-grains, fine μ precipitates and lattice defects including dislocations, stacking faults, and Lomer-Cottrell locks. The formation of low-density semi-coherent μ precipitates also minimize the loss of ductility and enhance the strengthening to some extent.

(3) The manufacturing technique using selective laser melting offers a new strategy in materials design for improving the mechanical properties of CoCrNi-based precipitation-strengthening alloy.

Acknowledgement

Financial support from the National Key Research and Development Program of China (Grant No. 2020YFB0311300ZL), and National Natural Science Foundation of China (Grant No. 52071343) are gratefully acknowledged.

References

[1] H. Huang, J.Y. Wang, H.L. Yang, S.X. Ji, H.L. Yu, Z.L. Liu, Strengthening CoCrNi

- medium-entropy alloy by tuning lattice defects, *Scripta Mater.* 188 (2020) 216–221.
- [2] B. Gludovatz, A. Hohenwarter, K.V.S. Thurston, H. Bei, Z. Wu, E.P. George, R.O. Ritchie, Exceptional damage-tolerance of a medium-entropy alloy CrCoNi at cryogenic temperatures, *Nat. Commun.* 7 (2016) 10602–10609.
- [3] Z. Zhang, H. Sheng, Z. Wang, B. Gludovatz, Z. Zhang, E.P. George, Q. Yu, S.X. Mao, R.O. Ritchie, Dislocation mechanisms and 3D twin architectures generate exceptional strength-ductility-toughness combination in CrCoNi medium-entropy alloy, *Nat. Commun.* 8 (2017) 14390.
- [4] G. Laplanche, A. Kostka, C. Reinhart, J. Hunfeld, G. Eggeler, E.P. George, Reasons for the superior mechanical properties of medium-entropy CrCoNi compared to high-entropy CrMnFeCoNi, *Acta Mater.* 128 (2017) 292–303.
- [5] J.S. Miao, C. Slone, S. Dasari, M. Ghazisaeidi, R. Banerjee, E.P. George, M.J. Mills, Ordering effects on deformation substructures and strain hardening behavior of a CrCoNi based medium entropy alloy, *Acta Mater.* 210 (2021) 116829.
- [6] J.Y. Wang, H.L. Yang, J.M. Ruan, Y. Wang, S. Ji, Microstructure and properties of CoCrNi medium-entropy alloy produced by gas atomization and spark plasma sintering, *J. Mater. Res.* 34 (12) (2019) 1–11.
- [7] I. Moravick, L. Gouvea, J. Cupera, I. Dlouhy, Preparation and properties of medium entropy CoCrNi/boride metal matrix composite, *J. Alloys Compd.* 5 (2018) 979–988.
- [8] J.Y. Wang, H.L. Yang, H. Huang, J.M. Ruan, S. Ji, *In-situ* Mo nanoparticles strengthened CoCrNi medium entropy alloy, *J. Alloys. Compd.* 798 (2019) 576–586.
- [9] W.H. Liu, Z.P. Lu, J.Y. He, J.H. Luan, Z.J. Wang, B. Liu, Y. Liu, M.W. Chen, C.T. Liu, Ductile CoCrFeNiMo_x high entropy alloys strengthened by hard intermetallic phases, *Acta Mater.* 116 (2016) 332–342.
- [10] K.S. Ming, X.F. Bi, J. Wang, Precipitation strengthening of ductile Cr₁₅Fe₂₀Co₃₅Ni₂₀Mo₁₀ alloys, *Scripta Mater.* 137 (2017) 88–93.
- [11] E.O. Olakanmi, R.F. Cochrane, K.W. Dalgarno, A review on selective laser sintering/melting (SLS/SLM) of aluminium alloy powders: Processing, microstructure, and properties, *Prog. Mater. Sci.* 74 (2015) 401–477.
- [12] R.D. Li, M.B. Wang, Z.M. Li, P. Cao, T.C. Yuan, H.B. Zhu, Developing a high-strength Al-Mg-Si-Sc-Zr alloy for selective laser melting: Crack-inhibiting and multiple strengthening mechanisms, *Acta Mater.* 193 (2020) 83–98.
- [13] H.L. Yang, Y.Y. Zhang, J.Y. Wang, Z.L. Liu, C.H. Liu, S.X. Ji, Additive manufacturing of a high strength Al-5Mg₂Si-2Mg alloy: Microstructure and mechanical properties, *J. Mater. Sci. Tech.* 91 (2021) 215–223.

- [14] W. Xu, M. Brandt, S. Sun, J. Elambasseril, Q. Liu, K. Latham, K. Xia, M. Qian, Additive manufacturing of strong and ductile Ti-6Al-4V by selective laser melting via in situ martensite decomposition, *Acta Mater.* 85 (2015) 74–84.
- [15] D.D. Dong, C. Chang, H. Wang, X.C. Yan, W.Y. Ma, M. Liu, S.H. Deng, J. Gardan, R. Bolot, H.L. Liao, Selective laser melting (SLM) of CX stainless steel: Theoretical calculation, process optimization and strengthening mechanism, *J. Mater. Sci. Tech.* 73 (2021) 151–164.
- [16] X.Q. Wang, L.N. Carter, B. Pang, M.M. Attallah, M.H. Loretto, Microstructure and yield strength of SLM-fabricated CM247LC Ni-Superalloy, *Acta Mater.* 128 (2017) 87–95.
- [17] Z.G. Zhu, Q.B. Nguyen, F.L. Ng, X.H. An, X.Z. Liao, P.K. Liaw, S.M.L. Nai, J. Wei, Hierarchical microstructure and strengthening mechanisms of a CoCrFeNiMn high entropy alloy additively manufactured by selective laser melting, *Scripta Mater.* 154 (2018) 20–24.
- [18] B.L. Han, C.C. Zhang, K. Feng, Z.G. Li, X.C. Zhang, Y. Shen, X.D. Wang, H. Kokawa, R.F. Li, Z.Y. Wang, P.K. Chu, Additively manufactured high strength and ductility CrCoNi medium entropy alloy with hierarchical microstructure, *Mater. Sci. Eng. A* 820 (2021) 141545.
- [19] P.D. Niu, R.D. Li, K.F. Gan, T.C. Yuan, S.Y. Xie, C. Chao, Microstructure, Properties, and Metallurgical Defects of an Equimolar CoCrNi Medium Entropy Alloy Additively Manufactured by Selective Laser Melting, *Metall. Mater. Trans. A* 52 (2021) 753–766.
- [20] R.B. Chang, W. Fang, H.Y. Yu, X. Bai, X. Zhang, B.X. Liu, F.X. Yin, Heterogeneous banded precipitation of (CoCrNi)₉₃Mo₇ medium entropy alloys towards strength–ductility synergy utilizing compositional inhomogeneity, *Scripta Mater.* 172 (2019) 144–148.
- [21] P. Nie, O.A. Ojo, Z. Li, Numerical modeling of microstructure evolution during laser additive manufacturing of a nickel-based superalloy, *Acta Mater.* 77 (2014) 85–95.
- [22] Z. Tong, X. Ren, J. Jiao, W. Zhou, Y. Ren, Y. Ye, E.A. Larson, J. Gu, Laser additive manufacturing of FeCrCoMnNi high-entropy alloy: Effect of heat treatment on microstructure, residual stress and mechanical property, *J. Alloy Compd.* 785 (2019) 1144–1159.
- [23] S.S. Al-Bermani, M.L. Blackmore, W. Zhang, I. Todd, The Origin of Microstructural Diversity, Texture, and Mechanical Properties in Electron Beam Melted Ti-6Al-4V, *Metall. Mater. Trans. A*, 41A (2010) 3422–3434.
- [24] W. Wu, S. Ni, Y. Liu, B. Liu, M. Song, Amorphization at twin-twin intersected region in FeCoCrNi high-entropy alloy subjected to high-pressure torsion, *Mater. Charact.* 127 (2017) 111–115.
- [25] X.L. Wu, Y.T. Zhu, Y.G. Wei, Q. Wei, Strong Strain Hardening in Nanocrystalline Nickel, *Phys. Rev. Lett.* 103 (2009) 205504.
- [26] L. Dupuy, M.C. Fivel, A study of dislocation junctions in FCC metals by an orientation dependent line tension model, *Acta Mater.* 50 (2002) 4873–4885.

- [27] J.Y. Wang, H.L. Yang, H. Huang, J.P. Zou, S.X. Ji, Z.L. Liu, High strength-ductility $\text{Co}_{23}\text{Cr}_{23}\text{Ni}_{23}\text{Mn}_{31}$ medium—entropy alloy achieved via defect engineering, *Mater. Sci. Eng. A* 796 (2020) 139974.
- [28] S. Yoshida, T. Bhattacharjee, Y. Bai, N. Tsuji, Friction stress and Hall-Petch relationship in CoCrNi equi-atomic medium entropy alloy processed by severe plastic deformation and subsequent annealing, *Scripta Mater.* 134 (2017) 33–36.
- [29] N. Hansen, Hall-Petch relation and boundary strengthening, *Scripta Mater.* 51 (2004) 801–806.
- [30] U.F. Kocks, H. Mecking, Physics and phenomenology of strain hardening: the FCC case, *Prog. Mater. Sci.* 48 (3) (2003) 171–273.
- [31] T. Zhang, H.G. Li, H. Gong, Y.X. Wu, A.S. Ahmad, X. Chen, Effect of rolling force on tensile properties of additively manufactured Inconel 718 and elevated temperatures, *J. Alloys. Compds.* 884 (2021) 161050.
- [32] M.D. Sangid, T. Ezaz, H. Sehitoglu, I.M. Robertson, Energy of slip transmission and nucleation at grain boundaries, *Acta Mater.* 59 (2011) 283–296.
- [33] Y.L. Zhao, T. Yang, Y. Tong, J. Wang, J.H. Luan, Z.B. Jiao, D. Chen, Y. Yang, A. Hu, C.T. Liu, J.J. Kai, Heterogeneous precipitation behaviour and stacking-fault-mediated deformation in a CoCrNi-based medium-entropy alloy, *Acta Mater.* 138 (2017) 72–82.